Editors' Suggestion

Ultrashallow heavily constrained quantum wells: The cradle for fully electrically controlled and microwave coupled quantum bits

Yiwen Zhang,[1,2,3] Zonghu Li,[4] Yuchen Zhou,[4] Yuhui Ren,[1,2] Jiahan Ke,[1,2] Jiale Su,[1,2] Yanpeng Song,[5] Jun Deng,[5] Yang Liu,[4] Runze Zhang,[4] Haiou Li,[4,3] Baochuan Wang,[4,3] Zhenhua Wu,[1,2] Jun Luo,[1,2] Zhenzhen Kong,[1,2,*] Gang Cao,[4,3,†] Guoping Guo,[4,3] Chao Zhao,[5] and Guilei Wang[1,5,3,‡]

[1]*Institute of Microelectronics, Chinese Academy of Sciences, Beijing 100029, People's Republic of China*
[2]*University of Chinese Academy of Sciences, Beijing 100049, People's Republic of China*
[3]*Hefei National Laboratory, University of Science and Technology of China, Hefei, Anhui 230088, People's Republic of China*
[4]*CAS Key Laboratory of Quantum Information, University of Science and Technology of China, Hefei 230026, People's Republic of China*
[5]*Beijing Superstring Academy of Memory Technology, Beijing 100176, People's Republic of China*

(Received 18 December 2023; accepted 28 March 2024; published 25 April 2024)

Ge/SiGe heterostructure quantum well structures based on Ge two-dimensional hole gas have become one of the most promising research directions for preparing spin quantum bits due to their low disorder and high mobility. In this study, high-quality virtual substrates were epitaxially grown on 8-in silicon substrates using reduced pressure chemical vapor deposition. The surface roughness of the samples was optimized by adjusting key parameters such as the thickness of the reverse gradient buffer layer and $Si_{1-x}Ge_x$ buffer layer. Based on the strain modulation of dislocation dynamics, high-quality strained quantum wells with a density of stress accumulation points (DSAP) of $0.301/\mu m^2$ and surface RMS roughness less than 3 nm were achieved. Ultimately, an ultrashallow heavily constrained and undoped quantum well with a well depth of 15 nm, in-plane compressive strain of $\varepsilon_\parallel = -1.19\%$, and a mobility of $3.382 \times 10^5\ cm^2/Vs$ was obtained. A novel characterization method for quantum wells was proposed based on the defined DSAP. The ultrashallow quantum well depth and higher compressive strain enable the quantum well to maintain a high effective g factor (up to 8.3), becoming the cradle for fully electrically controlled and microwave coupled quantum bits.

DOI: 10.1103/PhysRevMaterials.8.046203

I. INTRODUCTION

Recent theoretical developments have revealed that heterojunction quantum well structures based on Ge two-dimensional hole gas (2DHG) have become one of the most promising research directions for spin quantum bits due to their low disorder and intrinsic high mobility. Silicon-based quantum bits are quantum computing units that use electron/hole or nuclear spins [1] in silicon as quantum information carriers, which have the advantages of compatibility with existing semiconductor processes, scalability, long relaxation time, and high fidelity and are one of the most promising platforms for realizing large-scale quantum computing. Significant progress has been made in the past five years in germanium hole-gas qubits; in particular, they can offer a high degree of quantum dot tunability [2], fast and all-electrical driving [2], and Ohmic contacts to superconductors for hybrids [2]. In addition, germanium has progressed from the formation of stable quantum dots and quantum dot arrays [3] to demonstrations of single-qubit logic, long spin lifetimes [4,5], and the formation of a four-qubit quantum processor based on germanium hole spin quantum dots [6]. Silicon-based strained Ge quantum well-hole-gas qubits have become a pioneer material platform for silicon-based qubits due to their high mobility, light hole effective mass, and strong spin-orbit interaction [7,8]. The long manipulation time and high fidelity [9] needed by qubits put forward extremely high requirements on the quality of material quantum wells, and the level of mobility reflects the strength of remote impurity scattering on quantum wells [10], which will directly affect the quantum bit decoherence time and fidelity. Therefore, the level of mobility will directly reflect the quality of quantum wells from the material. Generally, high mobility means high-quality quantum wells with low disorder [11]. The growth of high-mobility, high-quality silicon-based strained Ge-hole-gas quantum wells is the only way to the future of semiconductor quantum computing [12].

Silicon-based strained Ge-hole-gas quantum wells can be divided into light strain, standard strained, and heavily strained quantum wells according to the strength of the compressive stress. The standard compressive strain quantum well ($\varepsilon_\parallel = -0.63\%$) has achieved a 2×2 bit processor array [4] because of its higher mobility and stronger orbit spin coupling (SOC) effect [1,13], which is now the mainstream direction of semiconductor quantum computing multibit integration research. Lightly strained quantum wells ($\varepsilon_\parallel > -0.63\%$) have been shown to be of great significance for faster qubit drives and topological quantum devices [10,11,14]. The compressive strain and potential barrier confinement in the heavily con-

*zhenzhenkong@ime.ac.cn
†gcao@ustc.edu.cn
‡guilei.wang@bjsamt.org.cn

strained quantum well ($\varepsilon_{\parallel} < -0.63\%$) can move the light hole energy band (LHs) to a higher energy band, and the holes limited in this quantum well at this time belong to the heavy hole (HHs) type. It plays an important role in the preparation of single-triplet qubits [15], but due to the large lattice mismatch of higher strains, it will inevitably lead to a decline in the quality of quantum wells, posing a great challenge to the dislocation dynamic growth mode of heteroepitaxial materials.

The quality of the quantum well is mainly affected by the following points. First, the roughness of the interface and surface and the rough surface will directly lead to fluctuation (crosshatch) and thus affect carrier transport in the subsequent growth of the quantum well [16–19]. The second is that the threading arms extend to the lower interface of the quantum well, which may pass through the quantum well during growth and deteriorate the crystal quality. Therefore, the ideal quantum well interface must have a uniform misfit dislocation grid (crosshatch), no obvious threading dislocations, and a smooth surface. The growth of high-quality standard-strained and heavily constrained hole-gas quantum wells is the subject of this study.

In this study, a virtual substrate was epitaxially grown on an 8-in silicon substrate by means of reduced pressure chemical vapor deposition (RPCVD). By adjusting key parameters such as the thickness and composition of each film layer, high-quality Ge quantum wells with different strains and different structure thicknesses are finally obtained. The research characterization results indicate that through the overall collaborative optimization of the quantum well structure, the threading dislocation density before the $Si_{1-x}Ge_x$ barrier layer is maintained below 10^6 cm^{-2}, and all the threading dislocations are annihilated before the quantum well. The surface roughness of the heavily constrained quantum well is controlled within 3 nm, which can effectively suppress segregation at the $Si_{1-x}Ge_x$/Ge QW interface. Finally, ultrashallow heavily constrained and shallow standard-strained quantum wells with strains of -1.19% and -0.61% were obtained. The roughness of the heavily constrained quantum well was controlled at approximately 3 nm, and a saturation mobility of 33.82×10^4 cm^2/Vs and an in-plane effective g factor of up to 8.2 were obtained through low-temperature magnetic transport testing at $T = 250$–650 mK.

II. RESULTS AND DISCUSSION

A. Growth of Ge/SiGe heterojunction structures with different strains

In this study, heterojunction intrinsic quantum wells with different strains were grown on 8-in silicon wafers using ASM epsilon reduced-pressure chemical vapor deposition (RP-CVD). Using germane mixed hydrogen (GeH_4 in H_2) and dichlorosilane (SiH_2Cl_2) as precursors, a Ge layer of approximately 1.7 μm was prepared as a virtual substrate by high- and low-temperature growth methods. Subsequently, high-temperature annealing at 820 °C for 20 min was performed to reduce the threading dislocation density and obtain better quality Ge epitaxial layer. The reverse grading $Si_{1-x}Ge_x$ ($0.8 > x > 0.75$) layer was grown later at 800 °C by keeping the GeH_4 flow constant and gradually reducing the SiH_2Cl_2 flow. To filter the remaining threading dislocations

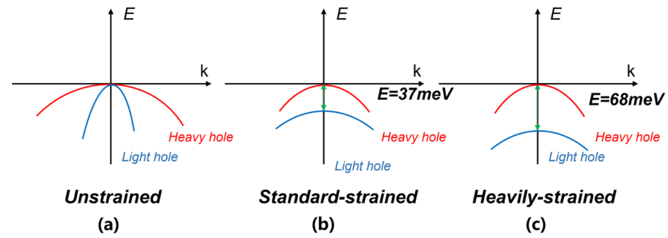

FIG. 1. (a) Unstrained QW. (b) Standard strained. (c) Heavily strained.

in the reverse grading layer, the dose of GeH_4 is increased while the temperature is lowered, and Ge-rich pulses are inserted to realize the synergistic optimization of the thickness of the reverse grading layer and the barrier layer. A constant composition $Si_{1-x}Ge_x$ buffer was grown at 650 °C, on which a 2DHG quantum well of thickness suitable for quantum computing was grown. Afterwards, a barrier layer of 15–40 nm on $Si_{1-x}Ge_x$ ($0.8 > x > 0.75$) was grown at a lower temperature, aiming at shielding remote impurity scattering from the sample surface while providing compressive stress. The final grown Si cap layer provides a good dielectric interface for device fabrication. Finally, we obtained sample A, sample B, and sample C. The samples correspond to sample A as a standard-strained sample [Fig. 1(b)] quantum well structure with a thicker reverse grading buffer layer and a thinner potential barrier buffer layer. Sample B is a standard-strained quantum well structure with a thinner reverse grading buffer layer and a thicker barrier buffer layer. Sample C is heavily constrained [Fig. 1(c)] quantum well structure. By using VASP, we can obtain the separation of the light and heavy hole energy bands (ΔE_{SOC}) of sample A and sample B as 37 meV and 68 meV.

B. Strained quantum well characterization and analysis of material and structure

The study used high-resolution x-ray diffraction (HR-XRD) and scanning transmission electron microscopy (STEM) to characterize the composition of the material and the degree of strain in detail. The interface morphology and dislocations at the quantum wells were characterized by etch pit density (EPD), scanning electron microscopy (SEM), and atomic force microscopy (AFM). The high-resolution imaging of the quantum well interface was carried out by HAADF, and the relative strain at the quantum well was characterized by the GPA system and HR-XRD.

1. *Strained quantum well characterization and analysis of material and structure*

The correlation between TDD and the size of 3D islands that form during the first stage of layer growth has been established [20]. Matthews proposed a mechanism for the formation of defects through the coalescing of initially isolated islands [21]. It was concluded that small rotational misalignments of these islands generate defects upon merging. These defects provide scattering centers and reduce carrier mobility, making methods of reducing TDD advantageous for device performance. Inserting a dislocation filter layer in the grown

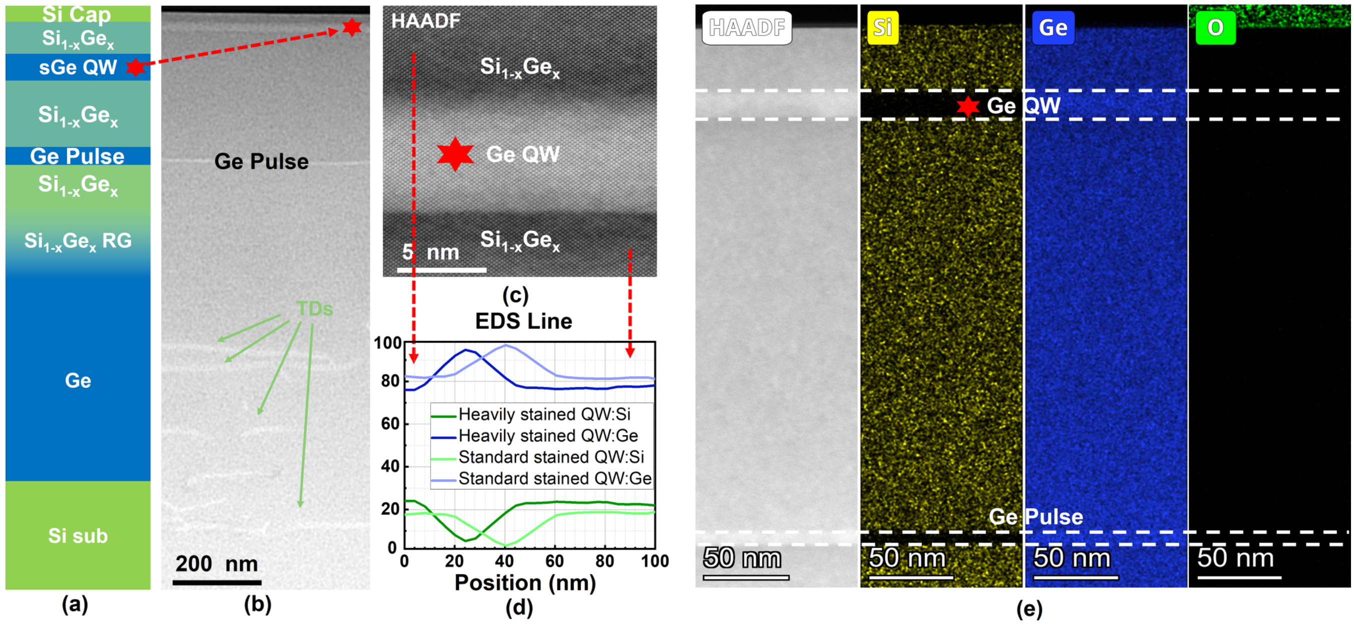

FIG. 2. Structural characterization of a Ge/SiGe heterostructure. (a) Ge/SiGe layer schematics (include Ge-rich pulse and TDs). (b) TEM of the Ge/SiGe heterostructure. (A Partial diagram of threading dislocation can be found in the Appendix, Fig. 11.) (c) HAADF of Ge/SiGe heterostructure (d) Heavily and standard Ge QWs with Ge (blue) and Si (green) concentration profiles by TEM/EDX line. (e) HAADF EDX mapping of Ge (blue), Si (yellow), and O (green) distribution.

structure will therefore cause a discontinuity in the lattice constant, which will generate a network of misfit dislocations. The misfit dislocation network provides a large interaction interface for defect growth. Driven by the mismatch stress of the dislocation filter layer, threading dislocations slip perpendicular to the growth direction and eventually collide and annihilate each other. It will be beneficial to increase the mobility of dislocations, provide interlayer relaxation, reduce the surface roughness of the upper interface, reduce the density of threading dislocations, and thus increase the mobility of quantum wells [22,23]. Yonenaga *et al.* found that when the composition of $Si_{1-x}Ge_x$ moves to pure Si, the stacking dislocation energy decreases, which means that the formation of stacking dislocations is easier [24]. Yonenaga's conclusions show that $Si_{1-x}Ge_x$ with a high $Si_{1-x}Ge_x$ component ($x > 0.6$) content will effectively reduce the generation of stacking dislocations compared to a $Si_{1-x}Ge_x$ buffer with a low Ge content. Therefore, moderately increasing the Ge content and reducing the growth temperature in the constant-composition $Si_{1-x}Ge_x$ layer after passing through the Ge-rich pulse layer can effectively reduce the generation of stacking dislocations. The Ge-rich pulse layer and its underlying film layer will provide tensile strain for the above $Si_{1-x}Ge_x$ barrier buffer [25]. Both of those effects effectively reduce the roughness at the interface of the quantum well, thereby increasing the mobility of the quantum well. In summary, this study inserted a Ge-rich pulse and then increased the constant composition $Si_{1-x}Ge_x$ layer to generate strain quantum wells. It has the following advantages: (i) The Ge-rich pulse peak is inserted at the end of the reverse grading buffer, realizing high-speed reverse grading in a narrow area. A large number of threading dislocations extending upward are annihilated, which acts as a dislocation filter layer [26]. (ii) The barrier buffer layer grown at low temperature more easily obtains a high-quality well interface because the low temperature reduces the adsorption rate of surface atoms, thereby inhibiting the surface roughening process and promoting a more ideal relaxation of the improved Frank-Read (MFR) mechanism [27]. (iii) The Ge-rich pulse layer and its underlying film layer increase a certain tensile strain for the upper layer, which contributes to the reduction in roughness [25]. (iv) Improving the Ge composition of the barrier layer after the Ge-rich pulse can increase the stacking fault energy, thereby reducing the generation of stacking faults in the barrier layer [24].

2. *Cross-sectional image results and analysis*

Figure 2(a) shows a schematic diagram of the Ge/SiGe heterojunction structure. Figure 2(b) shows TEM images of the whole layer of the structure. By counting the average density of threading dislocations, the threading dislocation density in the standard-strained quantum well structure (sample B) is $61.44/\mu m^2$, while the threading dislocation density in the heavily constrained quantum well structure (sample C) is $64.94/\mu m^2$, and the dislocation density is relatively increased. The reasons come from the following: (i) The thickness of the reverse grading buffer of the heavily constrained quantum well structure increases, resulting in more threading dislocations. (ii) The thickness of the heavily constrained quantum well structure barrier buffer is reduced, and the annihilation probability of threading dislocations extending upward from the reverse grading buffer is reduced in the barrier layer, leaving more threading dislocations. It can be seen from Fig. 2(b) that due to the combined effect of the Ge-rich pulse and the reverse gradient buffer layer beneath it, dislocations are effectively screened below the Ge-rich pulse. At this TEM magnification, no threading dislocations can be seen extending above the Ge-rich pulse. Under this TEM magnification,

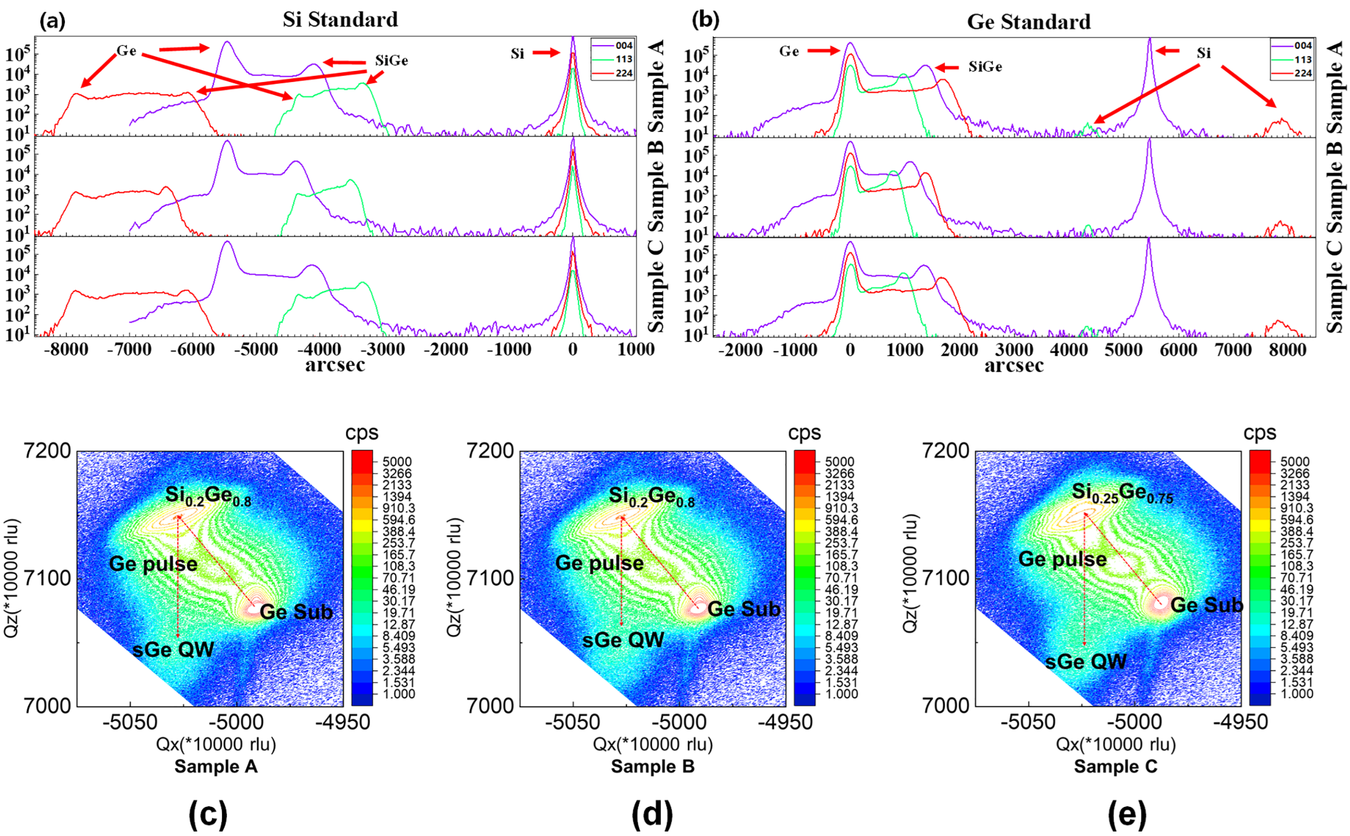

FIG. 3. HRXRD analysis of the Ge/SiGe heterostructure. (a), (b) Rocking curves of (004), (113) and (224). (c)–(e) RSM with sample A, sample B, and sample C.

no threading dislocations can extend above the Ge-rich pulse. Figure 2(c), 2(e) is an aberration-corrected (AC) high-angle annular dark-field scanning transmission electron microscopy (HAADF-STEM) image of the structure. The HAADF imaging results demonstrate a clear interface between the QW and the bottom barrier [28]. Since the dangling bond energy of Ge is lower than that of Si during epitaxial growth, the deposited Ge is preferentially deposited in Ge-rich places. When Ge quantum wells are deposited on SiGe, Ge atoms gather preferentially at the deposition interface, making the SiGe/Ge interface generally present a sharp and clear morphology. However, when a SiGe barrier layer is deposited on the Ge quantum well, a large amount of Ge will segregate to the Ge well, which will make it difficult to grow a sharp Ge/SiGe interface, and eventually the sharpness of the upper interface will be significantly weaker than that of the lower interface [29,30]. O ratio analysis shows that O has not diffused into the SiGe layer, and the Si cap and SiO_2 layers on the surface are sharply visible.

3. Strain result characterization and analysis

Figure 3(a) shows the XRD diffraction peak curves of the symmetric crystal orientation (004) and asymmetric crystal orientation (113 and 224) tested with Si as the reference peak. Due to the long distance and high intensity of the selected reference Si peak, it means that the relative shift of the Ge peak and the SiGe peak is not intuitively displayed. Therefore, in this study, XRD diffraction of symmetric and asymmetric crystal orientations was carried out using the calibrated Ge peak, and the results are shown in Fig. 3(b). The SiGe peaks of different samples are shifted in both symmetric and asymmetric diffraction crystals, indicating that the Ge well position is subjected to different degrees of compressive strain. As calculated by the MA, sample C is subject to a heavier compressive strain, which is in line with the expected growth of the material. Through peak comparison, the full width at half-maximum (FWHM) of the germanium well (004) XRD peaks of the three samples is similar to that of the germanium substrate, indicating that the germanium well layer has a high crystal quality.

Figures 3(c)–3(e) show the reciprocal space mapping of XRD. The reverse grading buffer is represented between the Si peak and the $Si_{1-x}Ge_x$ peak. The SiGe peak corresponds to the thickness of the $Si_{1-x}Ge_x$ barrier layer, and the strained Ge quantum wells are located directly below the SiGe peak. The RSM diagram extracts the XRD data through MATLAB software, using the following formula to convert the measured ω-2θ of the instrument into the Q spatial coordinate:

$$\mathrm{Q_x} = R[\cos\omega - \cos(2\theta - W)] \tag{1}$$

$$\mathrm{Q_z} = R[\sin\omega + \sin(2\theta - W)] \tag{2}$$

where

$$R = |K_H| = |K_O|. \tag{3}$$

After calculation, the relaxation between the SiGe virtual substrate layer and the $Si_{1-x}Ge_x$ barrier layer is shown in

TABLE I. Comparison of structural parameters and characterization results of samples A, B, and C.

	Thickness		
Layer	Sample A	Sample B	Sample C
SiGe RG	577 nm	546 nm	614 nm
SiGe barrier	506 nm	512 nm	413 nm
	Strain and Mismatch		
sGe QW	Sample A	Sample B	Sample C
Strain	−0.74%	−0.61%	−1.19%
Par.mismatch	3.54E4ppm	3.73E4ppm	3.42E4ppm
Perp.mismatch	4.44E4ppm	4.36E4ppm	4.61E4ppm
	Relaxation		
Layer	Sample A	Sample B	Sample C
Ge VS	104.79%	104.58%	103.39%
sGe QW	88.01%	91.09%	85.48%
SiGe barrier	111.14%	108.44%	108.35%

Table I, and the samples all have overrelaxation. On the one hand, the reason comes from the lattice mismatch caused by the thermal expansion coefficient; on the other hand, it comes from the $Si_{1-x}Ge_x$ reverse grading buffer, which makes the $Si_{1-x}Ge_x$ barrier layer obtain additional tensile strain. The Ge well and the $Si_{1-x}Ge_x$ barrier layer have the same horizontal coordinates (Q_x) as SiGe, which means that the Ge QW well and the $Si_{1-x}Ge_x$ barrier layer have the same in-plane lattice parameters, indicating that the lattice is perfectly matched at this time and subjected to complete compressive strain. The lattice constants of each film layer are obtained by the following formula:

$$a_{\parallel} = \frac{\sqrt{h^2 + k^2}}{Q_x} \tag{4}$$

$$a_{\perp} = \frac{\sqrt{l^2}}{Q_z}, \tag{5}$$

where (h, k, l) corresponds to the diffraction crystal plane.

The obtained parallel lattice constants $a_{\parallel}$ and perpendicular lattice constants $a_{\perp}$ can be used to obtain the relaxation rate, in-plane strain, parallel mismatch, and vertical mismatch of each film layer, as shown in Table I and Fig. 4. Samples B and C both reached the expected compressive strain. Further comparison shows that as the compressive strain increases, the parallel mismatch relative to the Si substrate will decrease, and the vertical mismatch will increase. This is because the increase in compressive strain further compresses the Ge QW lattice, which is closer to the lattice constant of the Si substrate, inevitably leading to a decrease in parallel mismatch. As the compressive strain increases, the relaxation rate of the quantum well relative to the Si substrate decreases, which is consistent with expectations.

Figure 5(a) is the geometric phase analysis (GPA) of the sample, which can intuitively reflect the microscopic strain of the sample. ε_{yy} at the well is a uniaxial tensile stress, indicating that the stress on the vertical yy plane, that is, the in-plane direction of the quantum well, is a biaxial compressive stress. There is no obvious stress distribution of ε_{xx} and ε_{xy} at the well, indicating regular lattice matching in the growth

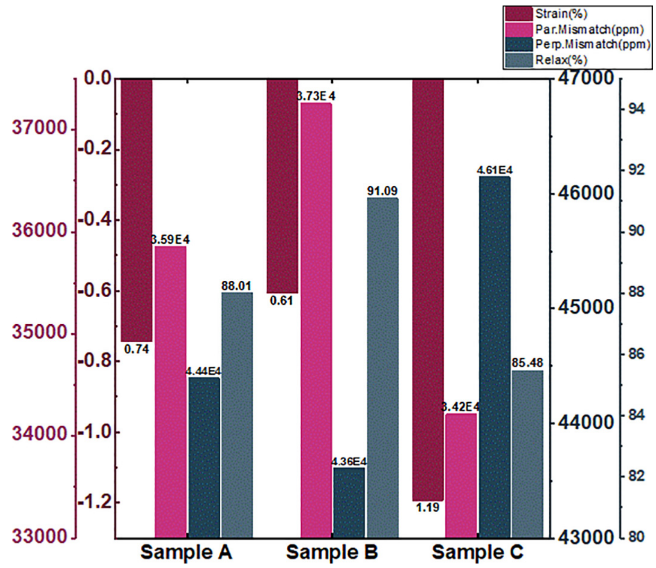

FIG. 4. The relaxation rate, in-plane strain, parallel mismatch, and vertical mismatch of sample A, sample B, and sample C.

direction. Figure 5(b) is the GPA strain + analysis diagram at the Ge-rich pulse peak, which shows that a Ge-rich high compressive strain narrow region is formed near the pulse peak, which will effectively filter threading dislocations.

4. *Surface roughness and threading dislocation characterization results and analysis*

Figure 6(a) shows the atomic force microscopy (AFM) surface topography of the sample. The feature topography is arranged along a staggered 45° to the X direction, forming grooves and ridges. It comes from the surface steps formed by the accumulation of 60° dislocations and is arranged along the $<110>$ surface orientation, which is in the same direction as the subsurface misfit dislocations, forming a clearly visible crosshatching. Dispersed uniform crosshatching is more conducive to slip annihilation of threading dislocations and prevents dislocation accumulation caused by local accumulation of mismatch strain. The formation principle comes from the strain relaxation competition mechanism caused by the modified Frank-Read (MFR) method. It can be known from first principles that compressive strain exerts negative energy on the surface. To balance the negative strain energy, the system fluctuates during the growth process to increase the surface area to increase the surface free energy of the system and finally restore the energy balance of the system [19]. Combined with the analysis in Table I, it can be concluded that: (i) As the growth position of the Ge-rich pulse peak advances, the thickness of the reverse grading buffer layer decreases, and the surface roughness of the sample decreases accordingly. This is because the shortening of the growth time of the reverse grading buffer layer prevents the atoms from reaching the position with higher surface energy during the growth process, thereby reducing the density and height of the surface islands and reducing the surface roughness. (ii) As the Ge-rich pulse peak advances, the thickness of the barrier layer increases, the annihilation rate of threading dislocations increases, and the surface roughness decreases. However, the

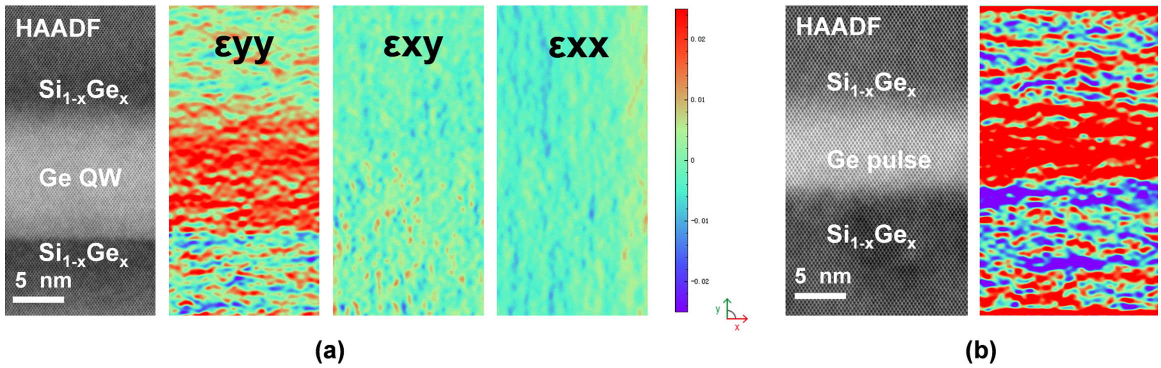

FIG. 5. GPA analysis of sample C about (a) germanium quantum wells and (b) Ge-rich pulses.

growth position of the Ge-rich pulse is not as early as possible. On the one hand, when the thickness of the reverse grading buffer layer is too low, the threading dislocations extending from bottom to top cannot be annihilated in the thin buffer layer, so large number of threading dislocations gather on the surface, resulting in a corresponding increase in roughness. On the other hand, if the barrier layer is grown far beyond the critical thickness, large number of misfit dislocations will be generated, which will also damage the quality of the quantum well interface. The results of the 2D Fourier transform on the AFM image obtained from the EPD on the sample surface are shown in Fig. 5(b). The main frequency of sample B is closer, indicating that the surface of sample B has the longest wavelength and the weakest strain accumulation.

To further characterize the quality of quantum wells, a selective etching pit chemical experiment was carried out using iodine-containing high germanium etchant ($HF:HNO_3:CH_3COOH:I_2 = 10$ ml : 20 ml : 100 ml : 30 mg). Because defects and dislocations bring a higher potential energy stress field, their increased surface energy potential will lead to an enhanced etching rate near the stress field. Selective etching will have an additional etching effect on the strain field sites generated by dislocations or mismatched lattice defects [31]. The etchant rate of samples with a high Ge composition etchant was obtained by a gradient control experiment. The results of SEM and TEM were used to confirm that the samples etched to the quantum well and the germanium-rich pulse were obtained, and then the etching

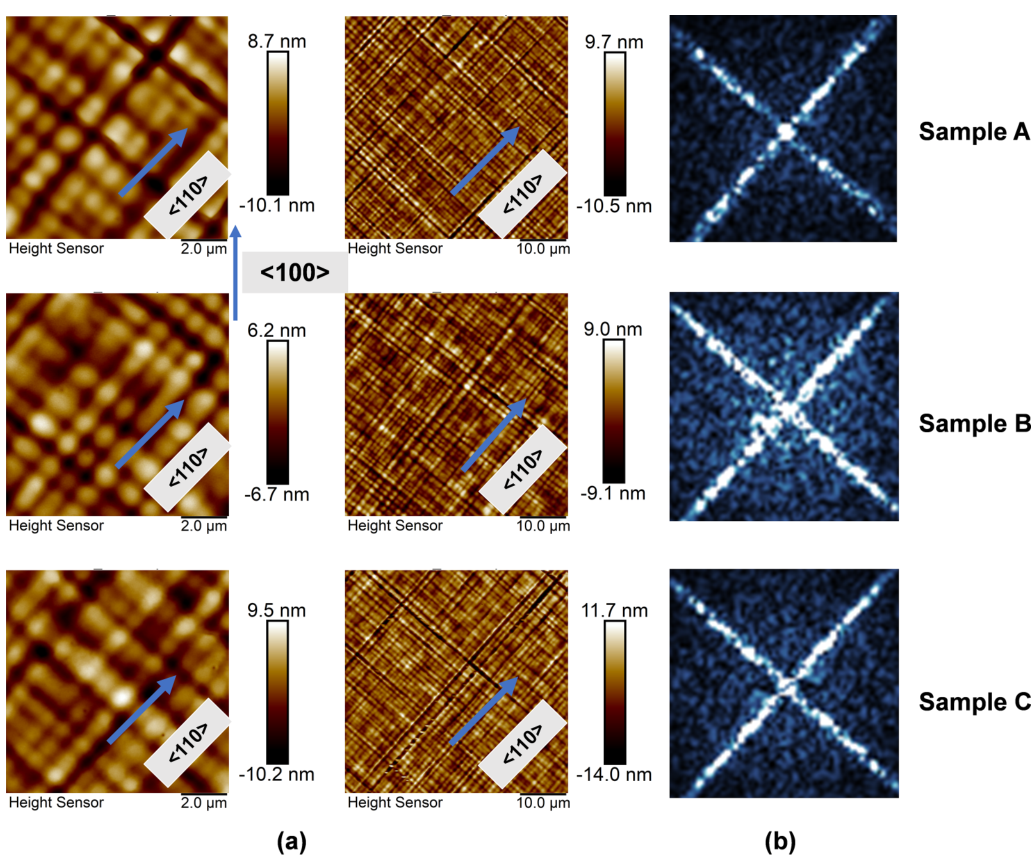

FIG. 6. (a) 10×10 μm and 50×50 μm AFM of sample A, sample B, and sample C. (b) 2D Fourier transform of the AFM.

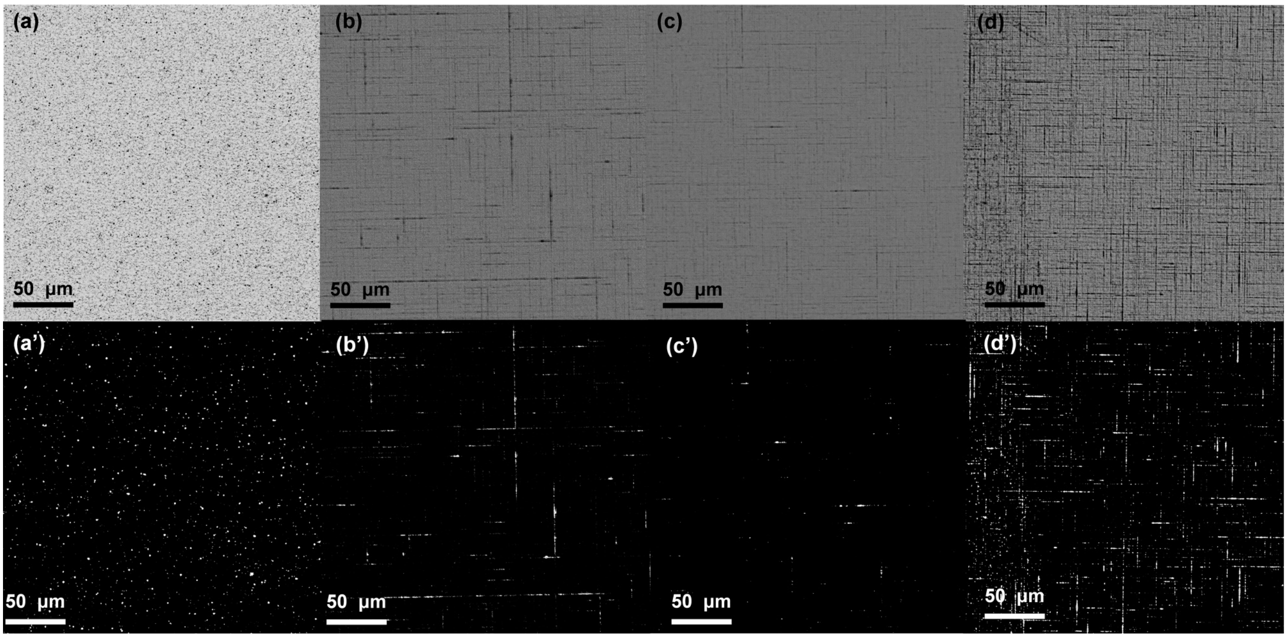

FIG. 7. (a) The microscope of the sample etched to below the Ge-rich pulse. The microscope of the sample etched to the Ge QWs with sample A, sample B, and sample C.

results were observed with an Olympus MX51 metallographic microscope.

Figure 7(a) is the microscope of the sample etched to below the Ge-rich pulse, in which there are large number of dot-shaped etch pits. Figures 7(b) and 7(c) show the patterns etched to the quantum wells of sample A, sample B, and sample C, respectively, and no dot corrosion pits appear. On the one hand, large number of threading dislocations are generated in the reverse grading buffer layer, and the annihilation rate of the dislocations increases greatly after passing through the Ge-rich pulse layer and the thicker barrier layer. On the other hand, due to the higher Ge content after the Ge-rich pulse peak and the higher degree of lattice matching, the generation rate of threading dislocation lines in the superstructure is greatly reduced. Therefore, compared with before the Ge-rich pulse, there is no obvious threading dislocation emergence point at the well. The comparison of Figs. 7(b)–7(d) shows that as the stress increases, the cross-stripe shadow becomes more obvious.

Etching will aggravate etching at stress accumulation [31]. The study uses PHOTOSHOP to filter the etched surface with color tolerance, extract the darker color position, and obtain the stress accumulation point patterns of Figs. 7(a′), 7(b′), 7(c′), and 7(d′). In Fig. 7(a′), the stress accumulation point (SAP) is in the shape of a dot, which is equivalent to the outcropping point of threading dislocation. In Figs. 7(b′), 7(c′), 7(d′), the stress gathering point is a cross-shaped depression, which represents the crosshatch intersection point and the deep groove position in the crosshatch. By comparison, it can be concluded that at the well position of sample ABC, there is no circular stress gathering point where threading dislocations are etched. Instead, they act as stress gathering points of cross stripes, which appear as gridlike uniform distributions. Combined with the strain of sample ABC, it can be found that with the increase in compressive strain at the well, the density and size of the stress accumulation points also increase correspondingly.

To confirm whether the threading dislocations at the wells are stacked and blocked at the intersection of the misfit dislocation grids during the slip, that is, whether the misfit dislocation grids at the wells generate a slip stress field sufficient to hinder the threading dislocations. This confirms whether there are threading dislocation line outcrops at the well interface. SEM was used to characterize the surface of the sample after EPD etching to the well and before the Ge-rich pulse. Figures 8(a) and 8(b) show the sample SEM and AFM etching below the Ge-rich pulse. Etching pits are formed on the surface, and inward etching is aggravated on the side of the pits. The round pits are surface defects caused by the outcropping of threading dislocations. The location of aggravated etching is along the threading dislocation line. Because of the lattice mismatch, the potential energy increases here, which accelerates the etching rate and forms a unidirectionally aggravated etch pit in the corrosion.

Figures 8(c), 8(d) show the SEM image of the material corroded to the quantum well. Instead of forming circular etch pits, as shown in Fig. 8(a), there are waves that aggravate corrosion along the crosshatching. The missing etched pits indicate that the threading dislocations are filtered, and there are no outcropping threading dislocations at the well. The waves are due to the close etch ratio of the crosshatched grooves and ridges, and the etch only deepens the original topography. Figures 8(e)–8(g) are the AFM characterization results of samples A, B, and C etched to the well, respectively. Surface fluctuations caused by stress relaxation leading to the staggered formation of surface grooves and ridges, and the stress at the interlaced stack of grooves and ridges is further concentrated, which has a higher etching ratio, forming the cross depression in the figure. Therefore, after the sample is etched, deep etching points, that is, stress accumulation points,

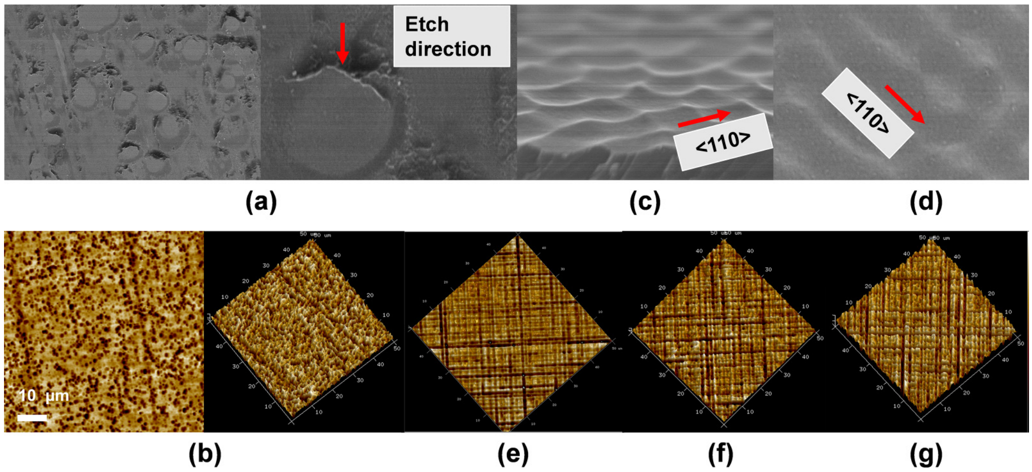

FIG. 8. (a) SEM image of the sample after etching under a Ge-rich pulse. (b) AFM etching below the Ge-rich pulse. (c) Cross section SEM images of samples etched to quantum wells. (d) SEM images of samples etched to quantum wells. (e)–(g) AFM images of sample A, sample B, and sample C etched to quantum wells.

appear. Whether the SAP is uniform will directly affect whether threading dislocations will be blocked by stacking, and its density reflects the density of crosshatching after straining at the well. The application of compressive stress makes the system more crosshatched to achieve relaxation. However, the increase in crosshatching brings about the overlapping of misfit dislocation grids, forming more stress accumulation points. In summary, the stress release and misfit dislocation blockage at the sample quantum well can be directly characterized by the density of stress accumulation points (DSAP). In Fig. 7, metallographic microscopy can only be used to qualitatively observe whether the SAP distribution is uniform. To obtain DSAP further quantitatively, the study proposes to use NANOSCOPE ANALYSIS software to analyze the AFM images of etched samples. Figure 9 shows the automatic counting pattern of SAP etched to the quantum well of sample ABC, and its DSAPs are 0.245/μm^2, 0.203/μm^2, and 0.301/μm^2. As seen in Fig. 9, the increase in the compressive strain of the quantum well will increase the DSAP and will also be accompanied by an increase in roughness. The uniform distribution of the SAP morphology confirmed that the crosshatching grid distribution of all samples was uniform, dislocation blocking did not occur, and the relaxation release mode was correct and did not cause surface wrinkles. The design structure effectively shields the threading dislocation lines extending upward from below and prevents stacking errors caused by grid blockage of misfit dislocations. The optimized scheme reduces the interface (remote impurity) scattering from the material structure and obtains higher-quality quantum wells with different strains.

C. Heavily constrained quantum well characterization and analysis of low-temperature transport

Hall bars were prepared using the ultrashallow heavily constrained quantum wells (sample C) mentioned earlier to investigate their low-temperature magnetic transport in the $< 110 >$ crystallographic channel direction. The analysis structure is shown in Fig. 10(a). The source and drain terminals are provided with a constant current of 100 nA through a lock in, and two lock ins are used to measure the U1L1 longitudinal resistance ρ_{xy} and L1L2 transverse resistance ρ_{xx}, respectively, to obtain the Hall quantum effect of the analyzed sample. The electrical transport characteristic curve is shown in Fig. 10(b): its voltage $V_{th} = -1.9$ V, and the opening current is approximately 5.9 nA, with a saturation voltage of $V_G = -2.5$ V. The turn-on curve is rel-

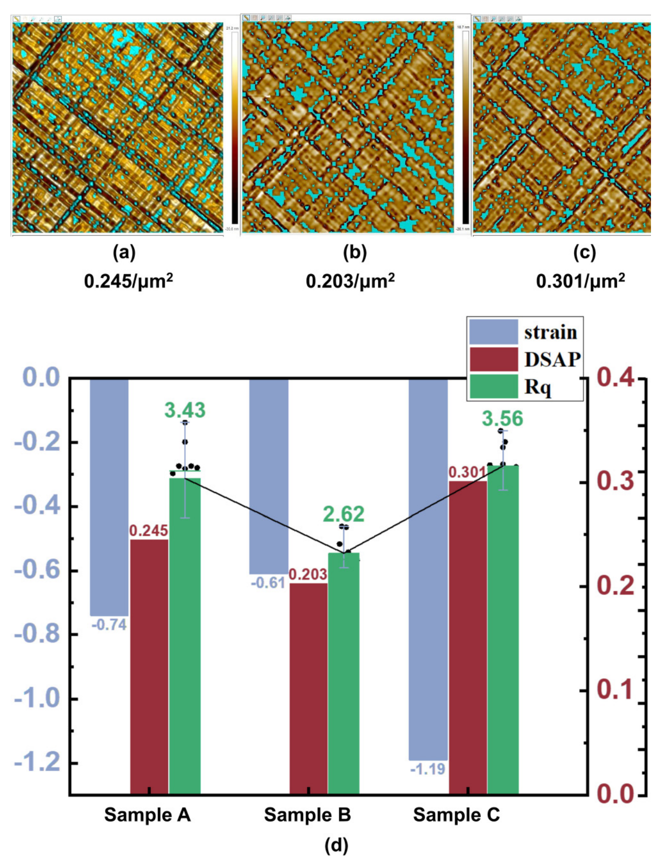

FIG. 9. (a)–(c) DSAP images of sample A, sample B, and sample C. (d) The strain, DSAP, and Rq of the three samples.

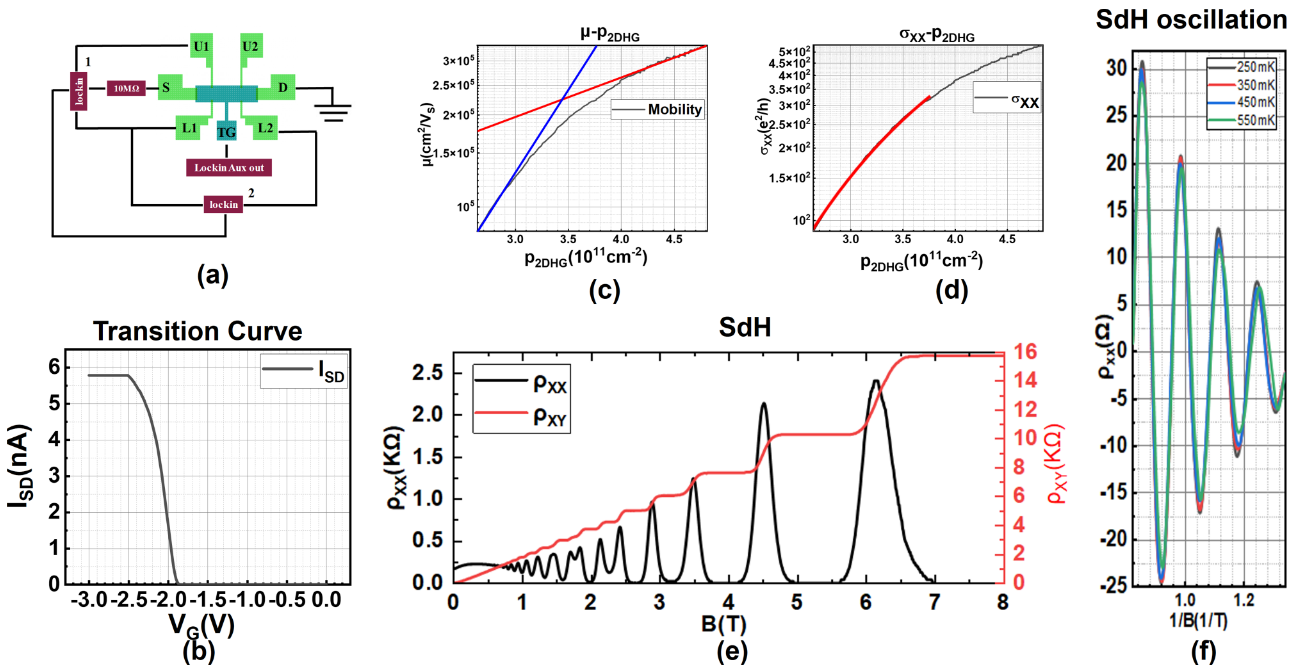

FIG. 10. Electrical and magnetotransport measurements of Hall-bar shaped HFET. (a) Four-terminal lock-in measurement circuit. The yellow area is the lock-in amplifier, the green area is the source and drain terminal, and the blue area is the top gate. (b) Transfer characteristic curve, $V_{sd} = 20\,\mu$V, $f = 230$ Hz. (c) Mobility μ vs carrier density p_{2DHG}. Black filled dots are data points. The blue curve is the fitting curve at low density. $\beta_{low} = 3.03 \pm 0.03$. The red curve is the fitting curve at high density. $\beta_{high} = 1.27 \pm 0.013$. The confidence levels of the two curves are both more than 0.999. (d) Longitudinal conductivity σ_{xx} vs carrier density p_{2DHG}. Black filled dots are data points. The red curve is fitted by $\sigma_{xx} \propto (p_{2DHG} - p_p)^p$, p=2. The confidence level is 0.999. (e) Quantum Hall effect curve at $p_{2DHG} = (4.466 \pm 0.087) \times\ 10^{11}\ \text{cm}^{-2}$. The Landau level integer filling factors ($\nu = 2 \sim 6$) and minimum of suspected fractional indication are labeled by blue numbers. (f) Temperature dependence of the Shubnikov-de Haas oscillations $\Delta\rho$ in the range T = 250–650 mK after background subtraction.

atively stable, reflecting a higher quality of the oxide layer, with only a small amount of defect level filling occurring. Figure 10(c) shows the relationship between the two-dimensional hole-gas density p_{2DHG} and mobility μ obtained through the classical Hall effect at 250 mK. In the high-density regime, due to the high interfacial-state density within the silicon dielectric, it is difficult to obtain a stable two-dimensional hole gas, so the highest mobility at high density cannot be determined [32]. From the graph, we can conclude that the critical density $p_c \approx 2.06 \times 10^{11}\ \text{cm}^{-2}$, while the stable carrier density is $4.84 \times 10^{11}\ \text{cm}^{-2}$. The stable saturation mobility was $\mu = 3.382 \times 10^5\ \text{cm}^2/\text{Vs}$. The mobility and density exhibit a power-law relationship $\mu \approx p^\alpha$. We used MATLAB to perform power-law exponential fitting analysis on low density and high density and obtained $\beta_{high} = 1.27$, with an index coefficient greater than 0.5 but less than 1.5, indicating that it is subject to multiple scattering mechanisms. One is that the higher DSAP at the quantum well leads to significant strain fluctuations, resulting in an increase in surface roughness, resulting in a power-law index below 1.5. The ultrashallow quantum well depth enhances the remote impurity scattering of surface interface states ($\alpha \sim 1.5$). The power-law index at low density $\beta_{low} \approx 3.03$ indicates that remote impurity scattering is the main scattering mechanism at low density [33]. In addition to characterizing the mobility and hole-gas density, p_p is the key to characterizing the low disorder of quantum wells, which is closely related to the formation of quantum bits. Figure 10(d) shows the transverse conductivity σ_{xx} of the Hall bar as a function of the hole-gas density p and the fitting curve for the percolation density $\sigma_{xx} \propto (p_{2DHG} - p_p)^p$, where the index 2 is determined for all two-dimensional systems. The fitting results show that the percolation density $p_p \approx 1.42 \times 10^{11}\text{cm}^{-2}$ is the lowest level in ultrashallow heavily constrained quantum wells, indicating that even under a barrier layer thickness below 15 nm and a large lattice mismatch, heavily constrained quantum wells still have low disorder and high material growth quality. Figure 10(e) shows ρ_{xx} (black) and ρ_{xy} (red) as a function of the vertical magnetic field B, with a maximum of 8T and $p_{2DHG} = 4.466 \times 10^{11}\text{cm}^{-2}$, $\mu = 3.059 \times 10^5\ \text{cm}^2/\text{Vs}$. We can observe clear Shubnikov-de Haas (SdH) resistivity oscillations above 500 mT. The starting points of Zeeman splitting are located at 1.7 T, and the periodic oscillations of ρ_{xx} and ρ_{xy} reflect the integer Hall quantum effects of different filling factors, indicating that the two-dimensional hole-gas material system with heavily constrained QW has become very clean. The occurrence of ρ_{xx} zeroing in 2 T indicates that there is no additional impurity magnetic resistance in the prepared device, and the quality of the oxide layer is high, resulting in lower interference to the two-dimensional hole gas in the ultrashallow heavily constrained quantum well. Figure 10(f) shows the temperature dependence of the normalized SdH amplitude at $p_{2DHG} = 3.72 \times 10^{11}\ \text{cm}^{-2}$. As the temperature increases, the oscillation of the low magnetic field classical Hall effect gradually disappears. Using the SdH differential oscillation temperature relationship, we can extract the effective hole mass of $m^* = 0.091m_0$. To determine the source of the multiple scattering mechanism, we calculated the quantum transmission lifetime $\tau_t = 14.55$ ps, quantum lifetime $\tau_q = 0.44$ ps, and Dinge ratio $\tau_t/\tau_q = 33.33$. This confirms that the main scattering sources of the heavily constrained quantum well are as follows: first, the stress accumulation points at the quantum well cause surface fluctuations, resulting in large angle scattering of the interface roughness; second, due to the ultrashallow depth of the quantum well, the interface state between silicon and the dielectric causes small angle scattering. Through the starting point of the quantum Hall effect and the starting point of Zeeman splitting in Fig. 10(e), we obtained that $g^* = 8.3$ at a high hole-gas density, which still has a large effective g factor, which is due to the greater separation of light and heavy hole energy bands caused by heavy strain. We point out here that due to the ultrashallow quantum well and wider SiGe/Ge interface, the hole wave function in the quantum well more easily experiences surface tunneling and leakage into the SiGe top barrier layer, which can be reflected in the higher percolation density and larger effective mass.

III. CONCLUSIONS

In summary, the study optimized and characterized the heterojunction structure through dislocation dynamics, resulting in the growth of ultrashallow heavily constrained quantum wells and standard-strained quantum wells. Among them, the parameters of the ultrashallow heavily constrained quantum well are as follows: DSAP is $0.301/\mu m^2$, RMS roughness is less than 3 nm, quantum well depth is 15 nm, in-plane compressive strain is up to -1.19%, and mobility is 3.382×10^5 cm^2/Vs. A more accurate strain characterization method for quantum wells has been proposed through the defined DSAP. Its ultrashallow quantum well depth and heavy compressive strain maintain a large effective in-plane g factor in the quantum well, providing a good material foundation for the full electrical manipulation of quantum dots and the microwave cavity coupling of quantum bits.

ACKNOWLEDGMENTS

Innovation Program for Quantum Science and Technology (Project ID. 2021ZD0302301). And Beijing Superstring Academy of Memory Technology has given strong technical and testing support.

Y.Z. carried out the device design and the experiments, analyzed device characteristics, and wrote/revised the manuscript with input from all authors, and measured at low temperature, analyzed device characteristics, and wrote/revised the manuscript. Z.L. fabricated the Hall bar transistors and revised the manuscript. Y.Z. participated in the analysis of the data. Y.R. participated in the analysis of the data. J.K. participated in the analysis of the data. J.S. participated in the analysis of the data. Y.S. participated in the analysis of the data. J.D. calculated band splitting. Y.L. participated in the analysis of the data. R.Z. participated in the analysis of the data. H.L. directed device analysis; revised the manuscript. J. Liu participated in the analysis of the data. B.W. provided the experiment platform and directed the experiments. Z.W. calculated band splitting. J. Luo directed the experiments. Z.K. directed the experiments and prepared the heterostructures materials. G.C. directed experiments and device design and analysis and revised the manuscript. G.G. provided the experiment platform and directed the experiments. C.Z. directed the experiments. G.W. supervised the material development and revised the manuscript and conceived and supervised the project.

The authors declare no conflict of interest.

APPENDIX: PARTIAL DIAGRAM OF THREADING DISLOCATION

Figure 11, as a partial image of Fig. 2(b) in the article, can be observed that almost all threaded dislocations (indicated by the green arrow) exist below the rich Ge pulse layer (indicated by the red arrow).

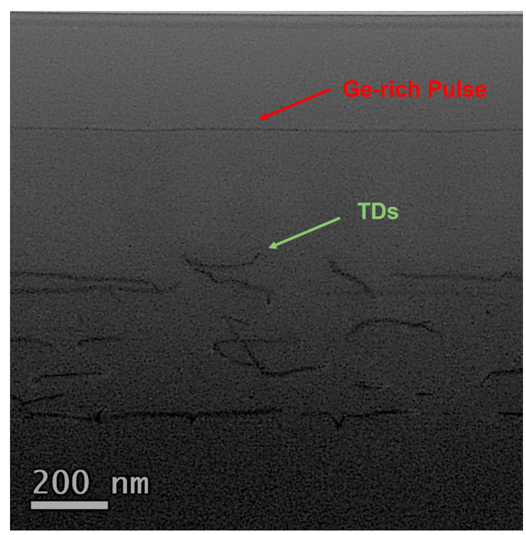

FIG. 11. Due to the combined effect of the Ge-rich pulse and the reverse gradient buffer layer beneath it, dislocations are effectively screened below the Ge-rich pulse. At this TEM magnification, no obvious threading dislocations can be found extending above the Ge-rich pulse.

[1] J. P. Dehollain, U. Mukhopadhyay, V. P. Michal, Y. Wang, B. Wunsch, C. Reichl, W. Wegscheider, M. S. Rudner, E. Demler, and L. M. K. Vandersypen, Nature (London) **579**, 528 (2020).

[2] N. W. Hendrickx, W. I. L. Lawrie, L. Petit, A. Sammak, G. Scappucci, and M. Veldhorst, Nature Commun. **11**, 3478 (2020).

[3] N. W. Hendrickx, D. P. Franke, A. Sammak, G. Scappucci, and M. Veldhorst, Nature (London) **577**, 487 (2020).

[4] N. W. Hendrickx, W. I. L. Lawrie, M. Russ, F. van Riggelen, S. L. de Snoo, R. N. Schouten, A. Sammak, G. Scappucci, and M. Veldhorst, Nature (London) **591**, 580 (2021).

[5] K. Wang, G. Xu, F. Gao, H. Liu, R.-L. Ma, X. Zhang, T. Zhang, G. Cao, T. Wang, J.-J. Zhang, D. Culcer, X. Hu, H.-W. Jiang, H.-O. Li, G.-C. Guo, and G.-P. Guo, Nature Commun. **13**, 206 (2022).

[6] G. Scappucci, C. Kloeffel, F. A. Zwanenburg, D. Loss, M. Myronov, J. J. Zhang, S. De Franceschi, G. Katsaros, and M. Veldhorst, Nature Rev. Mater. **6**, 926 (2021).

[7] P. Del Vecchio, M. Lodari, A. Sammak, G. Scappucci, and O. Moutanabbir, Phys. Rev. B **102**, 115304 (2020).

[8] A. Sammak, D. Sabbagh, N. W. Hendrickx, M. Lodari, B. Paquelet Wuetz, A. Tosato, L. Yeoh, M. Bollani, M. Virgilio, M. A. Schubert, P. Zaumseil, G. Capellini, M. Veldhorst, and G. Scappucci, Adv. Funct. Mater. **29**, 1807613 (2019).

[9] W. Huang, C. H. Yang, K. W. Chan, T. Tanttu, B. Hensen, R. C. C. Leon, M. A. Fogarty, J. C. C. Hwang, F. E. Hudson, K. M. Itoh, A. Morello, A. Laucht, and A. S. Dzurak, Nature (London) **569**, 532 (2019).

[10] M. Lodari, N. W. Hendrickx, W. I. L. Lawrie, T.-K. Hsiao, L. M. K. Vandersypen, A. Sammak, M. Veldhorst, and G. Scappucci, Mater. Quant. Technol. **1**, 011002 (2021).

[11] M. Lodari, O. Kong, M. Rendell, A. Tosato, A. Sammak, M. Veldhorst, A. Hamilton, and G. Scappucci, Appl. Phys. Lett. **120**, 122104 (2022).

[12] W. I. L. Lawrie, H. G. J. Eenink, N. W. Hendrickx, J. M. Boter, L. Petit, S. V. Amitonov, M. Lodari, B. Paquelet Wuetz, C. Volk, S. G. J. Philips, G. Droulers, N. Kalhor, F. van Riggelen, D. Brousse, A. Sammak, L. M. K. Vandersypen, G. Scappucci, and M. Veldhorst, Appl. Phys. Lett. **116**, 080501 (2020).

[13] W. J. Hardy, C. T. Harris, Y. H. Su, Y. Chuang, J. Moussa, L. N. Maurer, J. Y. Li, T. M. Lu, and D. R. Luhman, Nanotechnol. **30**, 215202 (2019).

[14] L. A. Terrazos, E. Marcellina, Z. Wang, S. N. Coppersmith, M. Friesen, A. R. Hamilton, X. Hu, B. Koiller, A. L. Saraiva, D. Culcer, and R. B. Capaz, Phys. Rev. B **103**, 125201 (2021).

[15] D. Jirovec, A. Hofmann, A. Ballabio, P. M. Mutter, G. Tavani, M. Botifoll, A. Crippa, J. Kukucka, O. Sagi, and F. Martins, Nature Mater. **20**, 1106 (2021).

[16] E. A. Fitzgerald, A. Y. Kim, M. T. Currie, T. A. Langdo, G. Taraschi, and M. T. Bulsara, Mater. Sci. Eng. B **67**, 53 (1999).

[17] E. A. Fitzgerald and S. B. Samavedam, Thin Solid Films **294**, 3 (1997).

[18] E. A. Fitzgerald, Y. H. Xie, M. L. Green, D. Brasen, A. R. Kortan, Y. J. Mii, J. Michel, B. E. Weir, L. C. Feldman, and J. M. Kuo, MRS Online Proceedings Library **220**, 211 (1991).

[19] V. A. Shah, A. Dobbie, M. Myronov, and D. R. Leadley, J. Appl. Phys. **107**, 064304 (2010).

[20] W. Pan, H. L. Stormer, D. C. Tsui, L. N. Pfeiffer, K. W. Baldwin, and K. W. West, Phys. Rev. Lett. **90**, 016801 (2003).

[21] J. W. Matthews and A. E. Blakeslee, J. Cryst. Growth **27**, 118 (1974).

[22] J. Matthews, Philos. Mag. **6**, 1347 (1961).

[23] J. Matthews, Philos. Mag. **13**, 1207 (1966).

[24] I. Yonenaga, S.-H. Lim, and D. Shindo, Philos. Mag. Lett. **80**, 193 (2000).

[25] Y. H. Xie, G. H. Gilmer, C. Roland, P. J. Silverman, S. K. Buratto, J. Y. Cheng, E. A. Fitzgerald, A. R. Kortan, S. Schuppler, M. A. Marcus and P. H. Citrin, Phys. Rev. Lett. **73**, 3006 (1994).

[26] T. Ward, A. M. Sánchez, M. Tang, J. Wu, H. Liu, D. J. Dunstan, and R. Beanland, J. Appl. Phys. **116**, 063508 (2014).

[27] F. LeGoues, B. Meyerson, J. Morar, and P. Kirchner, J. Appl. Phys. **71**, 4230 (1992).

[28] Y.-X. Li, Z. Kong, S. Hou, G. Wang, and S. Huang, Phys. Rev. B **108**, 045303 (2023).

[29] M. Copel and R. M. Tromp, Appl. Phys. Lett. **58**, 2648 (1991).

[30] E. Rudkevich, F. Liu, D. E. Savage, T. F. Kuech, L. McCaughan, and M. G. Lagally, Phys. Rev. Lett. **81**, 3467 (1998).

[31] B. Kolbesen, D. Possner, and J. Maehliss, ECS Trans. **11**, 195 (2007).

[32] Z. Kong, Z. Li, G. Cao, J. Su, Y. Zhang, J. Liu, J. Liu, Y. Ren, H. Li, and L. Wei *et al.*, ACS Appl. Mater. Interfaces **15**, 28799 (2023).

[33] C.-T. Huang, J.-Y. Li, K. S. Chou, and J. C. Sturm, Appl. Phys. Lett. **104**, 243510 (2014).